

Source Process of the Chi-Chi Earthquake: A Joint Inversion of Strong Motion Data and Global Positioning System Data with a Multifault Model

by Changjiang Wu, Minoru Takeo, and Satoshi Ide

Abstract The Chi-Chi, Taiwan, earthquake of 21 September 1999 was a large thrust earthquake that caused disastrous damage. The surface fracture trace runs along the Chelungpu fault, which strikes N5°E along most of the faulting area but turns to the northeast while approaching its northern end. It finally presents a horsetaillike faulting system and bends to an east-northeast direction at the northern end. Both strong-motion and Global Positioning System (GPS) data recorded large displacements in the northern part. In this study, we use a multifault model to simulate the observed large strong-motion and GPS data. The results of the joint inversion reveal that in the southern part, slip occurred mainly in the shallow portion, reaching a maximum about 20 m on the ENE fault, where the rupture propagated to the deep part of the fault. There was obviously slip vector rotation from south to north, such that the slip on the branched fault plane was almost purely reverse faulting. The seismic moment, a total of 2.7×10^{20} N m, was released in less than 40 sec during the mainshock. Aftershocks occurred mainly in areas where little or no slip occurred. Slip vector rotation can be explained by the complexity of regional tectonic stress. Changes in tectonic stress at the northern end of the fault inhibited the northward propagation of the rupture and favored the rupturing of the ENE fault.

Introduction

Taiwan is located at a convergent boundary between the Eurasian plate and the Philippine Sea plate (Fig. 1). The Philippine Sea plate subducts northwestward along the Ryukyu Trench, and the Eurasian plate underthrusts the Philippine Sea plate along the Manila Trench. The Philippine Sea plate moves northwestward at about 70–80 mm/yr (Seno, 1977, 1993; Yu *et al.*, 1999) relative to the Eurasian plate, creating the Taiwan collision zone. The collision started in Late Pliocene and is believed to be still vigorously taking place (Wu, 1978). Focal mechanism solutions are generally consistent with the southeast-to-northwest collision direction (Wu, 1978; Tsai, 1986; Rau *et al.*, 1996; Kao and Rau, 1999). The tectonic complexity accounts for very high seismicity, especially for earthquakes occurring on and off the eastern coast of Taiwan.

Looking at a map of Taiwan, one can distinguish five provinces from east to west: the Coastal Range, the Longitudinal Valley, the Central Range, the Western Foothills, and the Western Coastal Plain, which features a deep sedimentary layer. Tsai (1986) showed that thrust faults are dominant in the Western Foothills. As Suppe (1981) pointed out, compression within the Central Range and Western Foothills belt is dominated by slip in these thrust faults and related fault-bend folding within a wedge-shaped zone above a basal décollement. In fact, a large thrust earthquake did occur in the Western Foothills in 1963 (Wu, 1978).

The Chi-Chi earthquake (M_w 7.6), rupturing with a large thrust component, occurred in the Western Foothills of central Taiwan at 1:47 (local time) on 21 September 1999. Its epicenter, near the Chi-Chi town, was 23.85° N, 120.81° E, and its focal depth was 7 km, as determined by the Central Weather Bureau (CWB) using its routine earthquake monitoring network (Shin *et al.*, 2000). This was an unexpected earthquake because the background seismicity in this area is comparatively low (Ma *et al.*, 1999).

Surface ruptures from the mainshock extended about 85 km along the Chelungpu fault in a strike of about N5°E, with vertical displacement of 1–8 meters: the uplift roughly increases from south to north except for a small uplift in the middle. For the most part, the surface faulting trace runs nearly NS (Fig. 1). The trace turns to the NE in the northern part and to the ENE with a horsetaillike fault system at the northern end. Strong-motion data also show much larger displacement in the northern part of the faulting area than in the south. According to GPS observation (Central Geological Survey, 1999), horizontal displacements, ranging from 1.4 to 7 m in a NW direction, and vertical displacements, ranging from 1 to 4 m, are observed on the hanging wall, in contrast to a merely 0.3- to 0.5-m horizontal displacement (moving in a southeast direction) and 0.04- to 0.22-m vertical displacement on the footwall.

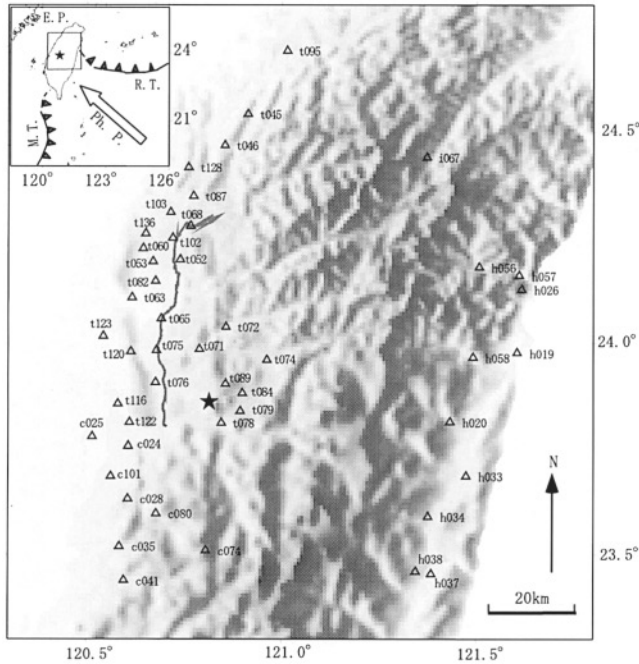


Figure 1. Tectonic settings, surface rupture trace (bold dashed line), and strong-motion station (triangle) distribution. The star marks the epicenter of the Chi-Chi earthquake. The arrow in the upper left illustration indicates the movement of the Philippine Sea plate (Ph. P.) relative to the Eurasian plate (E.P.). R.T. means the Ryukyu Trench, M.T. the Manila Trench.

Increasingly, strong-motion data are being used to reveal source processes of large earthquakes (e.g., Hartzell and Heaton, 1983, 1986; Takeo, 1985, 1987, 1992; Ide *et al.*, 1996; Hartzell *et al.*, 1996). The CWB has operated a dense network of digital strong-motion instruments (Shin *et al.*, 2000). This network consists of about 700 digital accelerographs in free-field sites. It may be the densest network in the world, with stations spaced only 3 km apart in the metropolitan areas. This network provided us with a wealth of high-quality strong-motion data. Meanwhile, the Central Geological Survey and the Institute of Earth Science, Academia Sinica, operate a dense GPS network to monitor some active faults in western Taiwan, such as the Chelungpu fault. They obtained the GPS coseismic deformation by comparing data with data from previous surveys. In this study, we invert strong-motion data and GPS data to identify the source process of the Chi-Chi earthquake.

Data

The accelerometer sensors used in this study, Teledyne Geotech Model A900 digital accelerometers with 16-bit and ± 2000 cm/sec² gain, have a flat response from DC to 50 Hz and a sampling frequency of 200 Hz (Liu *et al.*, 1999). Although the digital strong-motion seismographs provide low-noise, wide dynamic range, and high-quality waveform

records, there is still some baseline error due to instrumental fatigue or incompleteness. Iwan *et al.* (1985) showed that the baseline output of FBA-13/PDR-1, a typical strong-motion recorder/transducer, would shift by a very small amount whenever a sufficiently large input acceleration pulse was applied. They attribute this shift to the minute mechanical or electrical hysteresis within the transducer. Even for such a small shift, a velocity or displacement waveform integrated directly from such raw accelerograms without applying any preprocesses may deviate greatly from a zero baseline. Preprocesses to remove such baseline error have been proposed (Iwan *et al.*, 1985; Chiu, 1997). In this study, we employ Iwan's method, which is as follows. We first remove the DC offset, then determine the final offset of the acceleration from the velocity record. We remove the hysteresis offset by simply assuming that the hysteresis accumulates linearly between the first and last accelerations larger than 50 gal. Hence, a rectangular acceleration correction is adequate in this case. Besides its simplicity, Iwan's method is based on the hysteretic nature of the anomaly observed in their tests. More importantly, no high-pass filter is applied in this preprocess, such that we can get permanent DC component displacements from those (Fig. 2), although we ultimately high-pass filter the velocity records prior to inversion.

Strong-motion data from a total of 47 stations (Fig. 1) and GPS data from 60 GPS stations (Fig. 3) are used in our joint inversion. Considering the effect of the western sedimentary layer, we avoid using those strong-motion data recorded at the stations lying on the footwall far from the surface rupture trace. Fortunately, there are enough strong-motion records to allow for this choice, and we select strong-motion data recorded at only those stations that are close to the rupture trace among those on the footwall. All stations lying on the hanging wall are included in our inversion analysis. We also choose 10 stations on the eastern side of Taiwan to maintain good station coverage.

We apply the preprocessing to correct the baseline, then integrate the strong-motion data into velocity waveforms. By comparing those waveforms with each other, we find that the polarities of the TCU074 vertical component, CHY80 vertical component, CHY101 east–west component, HWA033 east–west component, and TCU136 east–west component are inconsistent with those of nearby stations. We therefore reverse the polarities of those records. We apply a 0.016–0.5 Hz bandpass filter to 50-sec velocity waveforms with a sampling frequency of 2 Hz. The number of total waveform data points is 14,100.

The GPS resurvey was carried out just one day after the mainshock occurred. Before the Chi-Chi earthquake, GPS observations for crustal deformation studies have been annually carried out in the Taiwan area since early 1990 (Yu *et al.*, 1997, 1999). The reobserved GPS data are compared with the results of previous surveys to obtain the coseismic deformation. We used 60-station GPS data with three components at each station. Some of the GPS data used in this

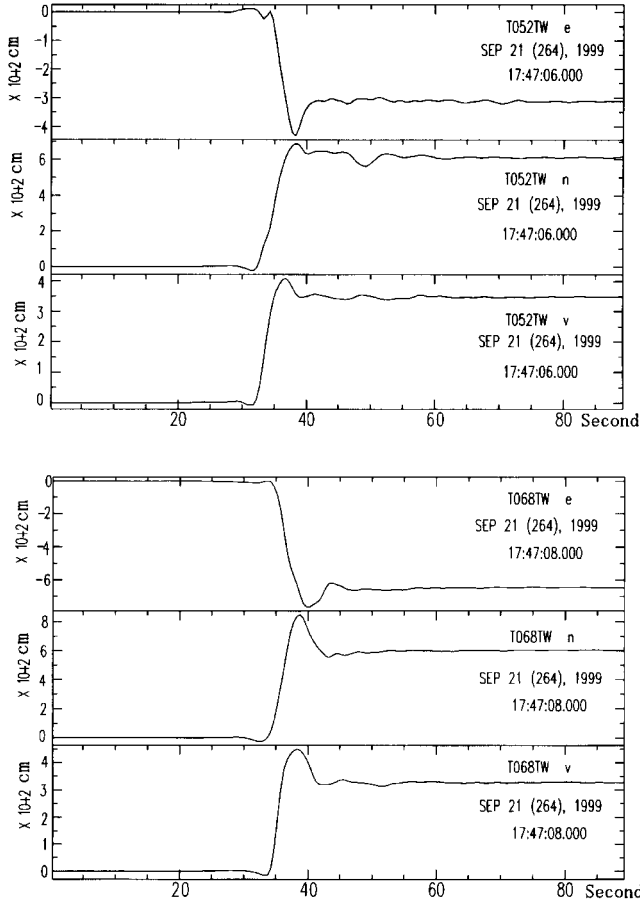


Figure 2. Displacement waveforms (the largest displacement) integrated from the preprocessed acceleration seismograms at stations t052 and t068.

study were kindly supplied by Professor Shui-Beih Yu (personal comm., 2000), while we also used some data distributed on the Website of the Central Geological Survey (Central Geological Survey, 1999), referring to some station locations listed by Yu *et al.* (1997). These values are listed in Table 1 with the station locations. We give a weight of 1 to GPS data during inversion, based on the ABIC criteria, which are explained in the following section.

Method

Ide and Takeo (1997) basically developed the inversion method used in this study, but we use not only the strong-motion records but also GPS data to reveal the rupture process. First we provide a sketch of the inversion method.

A subfault discretization system is convenient for the representation of spatial distribution of slip, and it is widely used in inversion analysis (e.g., Takeo 1992, Yoshida 1992). However, Ide and Takeo (1997) employed a more general representation of slip using 2D spatial and temporal basis functions (Fig. 4), with the expansion coefficients being un-

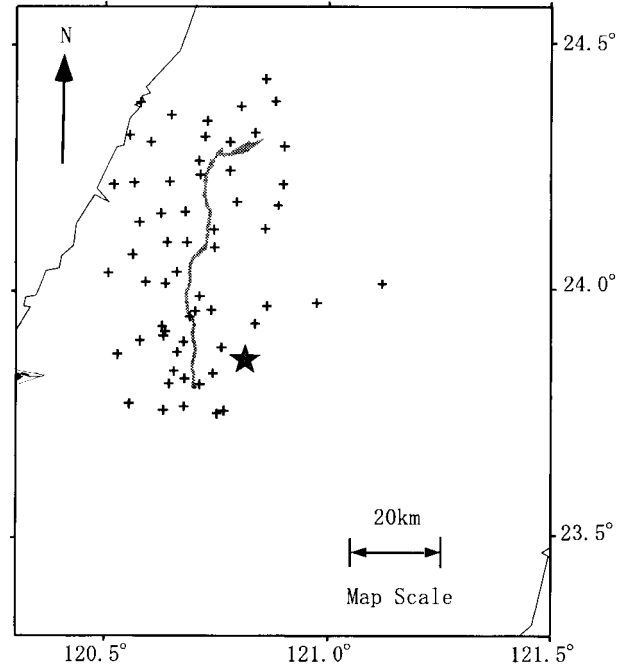


Figure 3. GPS station map (cross mark). The star marks epicenter of the Chi-Chi earthquake. The surface rupture trace is shown by the bold dashed line.

known parameters. The spatiotemporal distribution of slip rate is written as

$$\dot{u}_i(t) = \sum a_{ilmn} \phi_l^1(x_1) \phi_m^2(x_2) \psi_n(t) \quad (1)$$

where a_{ilmn} are the expansion coefficients and $\phi_l^1(x_1)$, $\phi_m^2(x_2)$, and $\psi_n(t)$ are the basis functions in strike direction, dip direction, and time, respectively. In this study, we use an isosceles triangle time window with a duration of 4 sec as the moment rate basis function. Each basis function for spatial expansion is also an isosceles triangle determined by three knots and controlling nine grid points. Each grid point alienates a 1-km interval and each knot alienates a 4-km interval.

The synthetic displacement at a station is represented as

$$u_j(x, t) = \iint g_{ij}(\mathbf{x}, t; \xi, \tau) \dot{u}_i(\xi, \tau) d\xi d\tau, \quad (2)$$

where $g_{ij}(\mathbf{x}, t; \xi, \tau)$ is a Green's function representing the j -th component of the synthetic displacement when an impulsive source in the i -th direction is applied at $\mathbf{x} = \xi$, $t = \tau$ (e.g., Aki and Richards, 1980). Substituting (1) into (2), the seismic wave displacement is written as

$$u_j^{\text{obs}}(\mathbf{x}, t) = \sum a_{ilmn} \iint g_{ij}(\mathbf{x}, t; \xi, \tau) \phi_l^1(\xi_1) \phi_m^2(\xi_2) \psi_n(\tau) d\xi d\tau + e_j(\mathbf{x}, t) \quad (3)$$

Table 1
The GPS Data Used in This Study

Latitude	Longitude	U_{NS} (cm)	U_{EW} (cm)	U_{nd} (cm)
24.2180	120.8990	453.7	-238.5	35.0
24.1260	120.8580	281.0	-182.0	130.6
23.9707	120.8620	178.5	-228.5	-75.4
23.9756	120.9739	128.8	-188.8	-59.5
23.9600	120.7020	344.0	-362.7	320.0
24.4314	120.8598	-33.6	21.8	-3.5
23.8126	120.6420	-18.5	74.0	-33.6
23.8778	120.6606	-22.0	83.0	-26.0
23.9197	120.6330	-21.0	78.0	-18.7
24.0996	120.6830	-51.0	96.0	-11.2
24.1623	120.6790	-48.0	81.5	-4.0
24.2376	120.7138	-49.0	84.4	-3.7
24.3130	120.7229	-50.0	52.0	-3.0
24.3464	120.7294	-47.0	42.7	-4.0
24.3867	120.8807	-49.0	23.0	-14.9
24.3842	120.5794	-18.3	24.8	7.2
24.0155	121.1197	69.0	-155.0	-50.0
24.1812	120.7947	572.9	-372.7	100.5
23.7721	120.5529	-6.5	31.7	-11.3
23.8731	120.5264	-6.9	29.6	-14.7
23.9004	120.5769	-12.8	44.0	-21.5
24.0390	120.5061	-11.5	30.5	-12.8
23.8982	120.6755	-32.7	86.7	-23.3
23.9097	120.6288	-19.7	65.0	-19.8
23.9483	120.6895	-35.2	108.9	-29.0
24.0168	120.6351	-28.4	78.7	-15.4
24.0996	120.6394	-35.6	70.6	-18.4
24.0398	120.6596	-39.9	96.8	-15.1
24.1583	120.6237	-33.2	58.2	-13.7
24.2178	120.5187	-16.2	31.4	-5.1
24.2208	120.5649	-22.0	38.6	-3.9
23.9616	120.7376	263.7	-387.5	203.8
23.9898	120.7115	326.1	-421.8	295.2
24.1249	120.7438	534.5	-404.0	415.0
24.2234	120.6432	-38.3	56.9	-10.1
24.0890	120.7452	411.3	-426.5	350.1
24.0199	120.5904	-18.9	57.6	-8.6
23.8872	120.7596	216.7	-267.2	171.3
23.9293	120.6266	-19.0	64.8	-18.3
23.7588	120.6298	-13.9	61.3	-18.9
23.8230	120.6778	-32.0	106.0	-23.1
23.7522	120.7500	98.9	-104.1	196.1
23.8119	120.7115	109.3	-279.0	323.5
23.8343	120.7424	210.0	-262.1	179.4
23.8384	120.6537	-25.5	78.3	-28.2
24.3168	120.5553	-19.5	29.5	4.7
24.2942	120.9014	-107.5	103.5	-24.3
24.1748	120.8870	301.7	-263.0	158.8
24.3031	120.7788	-54.6	55.4	6.5
24.2655	120.7111	-58.7	67.4	-8.4
24.2456	120.7793	652.4	-275.0	301.1
23.7579	120.7663	75.2	-97.5	62.9
24.3031	120.6010	-24.9	36.2	3.7
23.7668	120.6769	-26.0	94.7	-23.1
24.3762	120.8036	-59.0	38.0	-10.0
24.3215	120.8355	-75.0	50.0	-10.0
23.9349	120.8356	170.0	-222.0	76.0
24.0751	120.5608	-18.5	44.7	-5.2
24.3581	120.6469	-28.2	31.6	-0.2
24.1399	120.5763	-22.3	46.7	-2.2

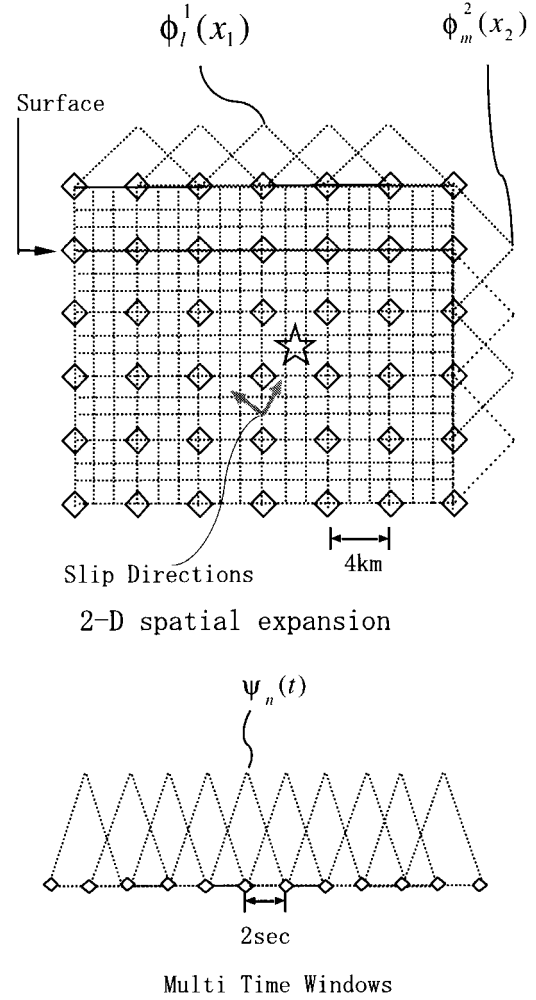


Figure 4. Illustration of knot distribution and isosceles multitime windows. The source is expressed as an expansion of isosceles time windows $\psi_n(t)$ and spatial windows $\phi_l^1(x_1)$, $\phi_m^2(x_2)$. Each window corresponds to an unknown source parameter (equation 1).

where $e_j(\mathbf{x}, t)$ is the error function between the observed and synthetic displacements. Then, we obtain an observational equation in vector form

$$\mathbf{d} = \mathbf{G}\mathbf{m} + \mathbf{e}_s \quad (4)$$

where \mathbf{d} , \mathbf{m} , and \mathbf{e} are the data vectors composed of sampled data, $u_j^{\text{obs}}(\mathbf{x}, n\Delta t)$, the parameter vector of a_{ilmm} , and the error vector of $e_j(\mathbf{x}, t)$, respectively. \mathbf{G} is an $N \times M$ (number of data \times number of parameters) matrix obtained after calculation integration in (3) and sampling corresponding to \mathbf{d} .

The surface deformations observed by GPS, \mathbf{d}_g , compose another observational equation, expressed as

$$\mathbf{d}_g = \mathbf{G}_g\mathbf{m} + \mathbf{e}_g \quad (5)$$

Employing an analytical expression of surface deformation

due to a finite rectangular fault deduced by Okada (1992), we can calculate each component of the matrix \mathbf{G}_g assuming that the model parameter a_{ilmm} represents a seismic moment released on a rectangular area surrounded by a knot interval. The analytical expression by Okada (1992) is for a half-space formulation. However, by comparing the static deformation calculated for the half-space and for the layered structure used in the calculation of synthetic seismograms, we find that the static deformation is not affected very much by the surface layers overlaying the half-space. Note that the error vector contains measurement errors and modeling errors. Although it is not necessarily so, for simplicity we assume that errors \mathbf{e}_s and \mathbf{e}_g are Gaussian with zero means and covariances $\sigma_s^2\mathbf{I}$ and $\sigma_g^2\mathbf{I}$, respectively, where \mathbf{I} is an identity matrix.

Following Ide *et al.* (1996), we introduce spatial (\mathbf{D}_s) and temporal (\mathbf{D}_t) smoothing constraints to maintain stability during inversion. Hence we can write those equations as

$$\begin{pmatrix} \mathbf{G} \\ \mathbf{G}_{\text{okada}} \\ \alpha_1\mathbf{D}_s \\ \alpha_2\mathbf{D}_t \end{pmatrix} \cdot \mathbf{m} = \begin{pmatrix} \mathbf{d} + \mathbf{e} \\ \mathbf{d}_g + \mathbf{e}_g \\ \mathbf{e}_1 \\ \mathbf{e}_2 \end{pmatrix}, \quad (6)$$

where we denote $\alpha_1 = \sigma/\sigma_1$, $\alpha_2 = \sigma/\sigma_2$ (here, $\sigma = \sigma_s$ or σ_g), $\mathbf{e}_1 = \sigma_1^2\mathbf{I}$, $\mathbf{e}_2 = \sigma_2^2\mathbf{I}$. The factors α_1 , α_2 are determined by Akaike's Bayesian information criterion (ABIC), which is formulated on the principle of maximizing entropy and defined as minus twice the marginal likelihood (Akaike, 1980). Refer to Ide *et al.* (1996) for details.

Models

Three velocity structures (Tables 2–4) are used in this study. We use the velocity structures in Tables 2 and 3 (Chen, 1995) for stations on the hanging wall and stations in eastern Taiwan, respectively. We modify the velocity structures originally derived for the Western Taiwan area (Chen, 1995) by adding three thin layers of low velocity according to the shallow crustal structure that was identified through short-period Rayleigh-wave dispersion data in southwestern Taiwan (Chung and Yeh, 1997). Since only *S*-wave velocities are given in Chung and Yeh's study, we calculate *P*-wave velocities assuming a Poisson's ratio of 0.25, that is, a *P*-wave velocity equal to 1.732 times the *S*-wave velocity.

To expand the spatiotemporal distribution on the assumed fault using isosceles triangle functions, the knots of such functions are arranged in the 3D spatiotemporal space, a 2D fault plane, and a time axis. The spatial distribution of knots is set at intervals of 4 km, and the knots in the time direction are set at intervals of 2.0 sec. For each point on the fault plane, these knots are activated after an imaginary rupture front with a propagation velocity of 3.0 km/sec reaches there. This rupture velocity determines only the initiation time of the rupture and the local rupture velocity between

Table 2
Layered Velocity Structures for Stations in Eastern Taiwan

V_p	V_s	Density	Depth	Q_p	Q_s
3.49	1.96	2.30	0.0	300.0	150.0
4.30	2.49	2.40	2.0	400.0	200.0
5.05	2.89	2.50	4.0	500.0	250.0
5.70	3.29	2.60	9.0	500.0	250.0
6.00	3.49	2.65	13.0	500.0	250.0
6.31	3.63	2.90	17.0	500.0	250.0
6.80	3.91	3.00	25.0	600.0	300.0
7.30	4.21	3.20	30.0	800.0	400.0
7.79	4.50	3.15	35.0	1000.0	500.0
8.18	4.79	3.20	50.0	1000.0	500.0
8.36	4.82	3.25	70.0	1000.0	500.0
8.19	4.73	3.25	140.0	1000.0	500.0
8.40	4.86	3.30	170.0	1000.0	500.0
8.70	5.09	3.30	240.0	1000.0	500.0

Table 3
Layered Velocity Structures Used for Stations on Hanging Wall

V_p	V_s	Density	Depth	Q_p	Q_s
3.61	2.04	2.30	0.0	500.0	250.0
4.66	2.73	2.40	2.0	500.0	250.0
5.45	3.16	2.50	4.0	500.0	250.0
5.76	3.39	2.60	9.0	600.0	300.0
6.15	3.58	2.70	13.0	600.0	300.0
6.26	3.59	2.80	17.0	800.0	400.0
6.71	3.89	2.90	25.0	1000.0	500.0
7.11	4.11	3.15	30.0	1000.0	500.0
7.50	4.32	3.15	35.0	1000.0	500.0
8.01	4.67	3.20	50.0	1000.0	500.0
8.27	4.77	3.25	70.0	1000.0	500.0
8.47	4.97	3.25	110.0	1000.0	500.0
8.31	4.84	3.25	140.0	1000.0	500.0
8.39	4.85	3.30	170.0	1000.0	500.0
8.51	4.92	3.30	200.0	1000.0	500.0
8.70	5.09	3.30	240.0	1000.0	500.0

Table 4
Velocity Structure Used for Footwall Stations.

V_p	V_s	Density	Depth	Q_p	Q_s
1.56	0.90	2.00	0.0	200.0	100.0
2.29	1.32	2.05	0.29	200.0	100.0
2.74	1.58	2.30	0.71	300.0	150.0
3.78	2.20	2.50	2.09	500.0	250.0
5.04	3.03	2.60	4.0	500.0	250.0
5.71	3.26	2.70	9.0	500.0	250.0
6.05	3.47	2.80	13.0	500.0	250.0
6.44	3.72	2.90	17.0	500.0	250.0
6.83	3.99	3.00	25.0	600.0	300.0
7.28	4.21	3.20	30.0	800.0	400.0
7.77	4.49	3.15	50.0	1000.0	500.0
8.16	4.72	3.25	90.0	1000.0	500.0
8.34	4.79	3.25	110.0	1000.0	500.0
8.20	4.74	3.25	140.0	1000.0	500.0
8.40	4.86	3.30	170.0	1000.0	500.0
8.70	5.09	3.30	240.0	1000.0	500.0

neighboring knots. A proper choice of the expansion coefficients enables a faster or a slower rupture than this velocity. The Green's function is computed by the discrete wave-number method (Bouchon, 1981) and reflection-transmission method (Kennet and Kerry, 1979), with a horizontally layered velocity structure assumed. The effect of anelasticity is included by introducing complex velocities (Takeo, 1985).

The focal mechanism solution using the first *P*-motion data has a strike of N5°E and a dip angle of 36° (Shin *et al.*, 2000). This strike direction is consistent with the surface rupture trace, which extends along the Chelungpu fault, a north-south-trending thrust fault dipping 25 to 30° to the east (Bonilla, 1999; Ma, 1999). Let us choose the fault plane along the surface rupture trace with a strike of N5°E (84 km long) and a dip angle of 30° (44 km wide), as our first fault model (model A, Fig. 5). Note that in the case of such a fault, station TCU087 and some GPS stations that actually

lie on the footwall are erroneously placed on the hanging wall. We introduce a second model (model B) to avoid this problem, that is, while most of the fault (72 km long) strikes the same direction as the first model, we let the fault turn to the northeast (strike N22°E, dip angle 31.1°, 12 km long) in the northern part, since the surface rupture trace does turn to the northeast in this area. As mentioned previously, however, at the northern end, surface rupture trace turns to a northeast-east direction and behaves complexly. We therefore introduce the third model (model C), which is model B with another fault added (strike N65°E, dip angle 25.0°, 12 km long, 24 km wide) to the second model. These three models are sketched in Figure 5. Parameters of these three models are listed in Table 5.

The focal mechanism at each knot is represented by the sum of two slip vectors with rakes of 35° and 125°, respectively (in case of the ENE fault, rakes of 45° and 135° are used) under the constraint that the slip amount can not be negative. The Green's function for each focal mechanism is calculated at a grid interval of 1 km and multiplied by an isosceles spatial window, which is weighted by the model parameter on each knot (Fig. 4).

Model Comparison

First we give the same smoothing factors to these three models and carry out joint inversion for each fault model. The GPS data fitting (Fig. 6) of model B is obviously improved compared with the data of model A, whereas waveforms have not been improved so much from model A to B (Fig. 7). Waveform fitting is evidently improved in model C, besides the good fitting of observed and synthetic GPS data. The slip distribution for each model (Fig. 8) is almost the same for most parts of the faulting area; ruptures occur

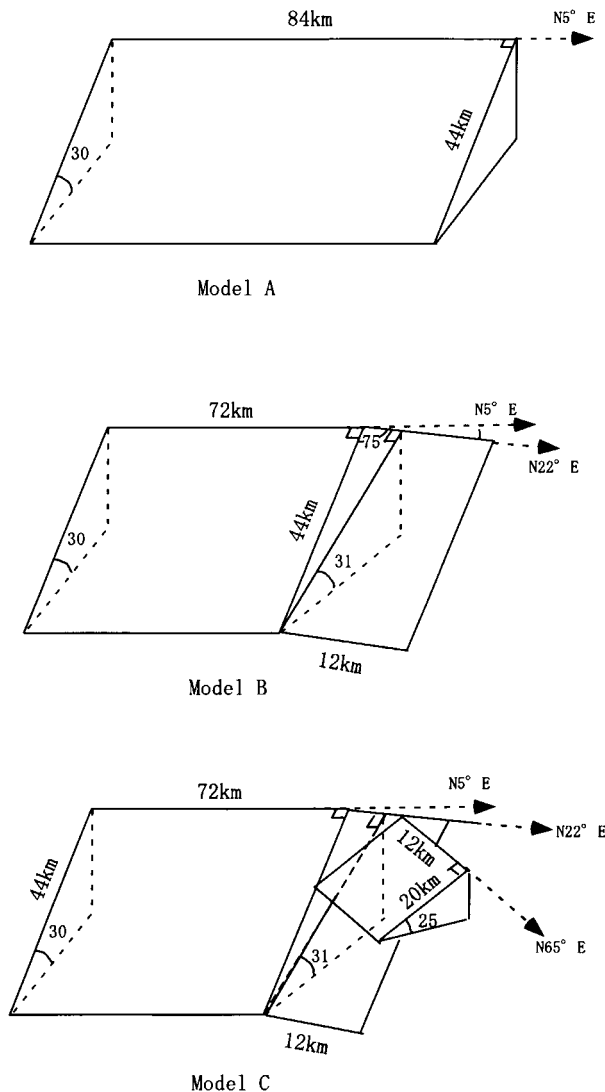


Figure 5. Fault model sketch map. The three fault models used in this article are shown.

Table 5

Parameters of the Three Fault Models Used in This Study

	Latitude	Longitude	Depth (km)
Hypocenter	23.86	120.81	7.25
Corners of the N5°E fault	23.56701	120.66172	0
(For model A)	24.31980	120.73802	0
	24.28991	121.11160	22.25
	23.53679	121.03960	22.25
Corners of the N5°E fault	23.56701	120.66172	0
(For model B and C)	24.21255	120.72350	0
	24.18232	121.10130	22.25
	23.53679	121.03960	22.25
Corners of the N22°E fault	24.21255	120.72350	0
	24.29599	120.76050	0
	24.18232	121.10130	22.25
	24.26577	121.13830	22.250
Corners of the ENE fault	24.26911	120.74864	0.
	24.31095	120.84710	0.
	24.17448	120.92490	10.25
	24.13264	120.82642	10.25

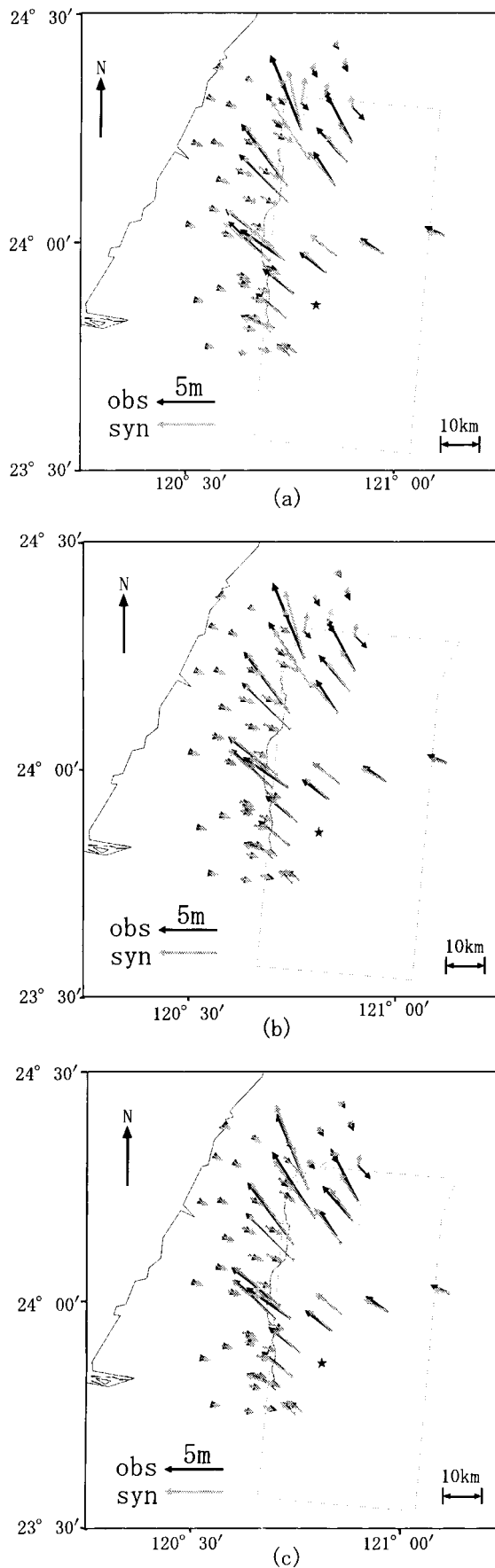


Figure 6. The GPS fitting corresponding to the three fault models. Dashed rectangles are the fault planes projected to the surface. The dark line along the western side of the dashed rectangles indicates the surface rupture trace. The epicenter of this main-shock is marked by an star. (a) Model A, (b) model B, (c) model C.

mainly in the shallow portion in the southern faulting area and reach a large amount of slip in the northern part; meanwhile ruptures propagate deeply into the north area. The largest slip occurs on the ENE fault in the case of model C. The slip distribution obtained from these three models is consistent with the surface rupture information mentioned previously.

Introducing the ENE fault improved the fitting of strong-motion and GPS data. The largest slip obtained by waveform and GPS data inversion on the ENE fault is consistent with the observed surface rupture. Therefore, we focus on model C in the following analysis.

The residual is obviously affected by the records obtained at the two stations (t052 and t068) with large amplitude in the northern faulting area. Considering the much larger amplitude of recorded ground motions in the northern part than in the southern part (Fig. 9), we adjust the weighting of waveforms at these two stations, and thereby obtain a spatial smoothing factor of 0.075 and a temporal smoothing factor of 0.8 as the final optimum result. Waveform fitting for stations lying on the hanging wall is much better than it is for stations on the footwall.

The final results show that ruptures occur mainly in the shallow portion (Fig. 10), with several distinguishable asperities from south to north but all lying shallower than 10 km deep. The largest slip (about 20 m) occurs on the north ENE strike fault, where the largest concentrations of fatalities were reported. Strong-motion station TCU068, lying on the ENE fault, recorded a dynamic displacement as large as 13 m and a static displacement of above 9 m (Fig. 2). Large ground deformation is also recorded by GPS observation in this area. It is reasonable to get such a large dislocation from strong-motion waveform and GPS data inversion.

In the shallow portion, slip vectors vary their orientations much more than they do in the deep portion (Fig. 11). In most of the faulting area, the reverse component is dominant, especially in the south area; however, slip vector rotation occurs in the north part. Note that slip vectors in the northern part rotate to the direction parallel to the dip direction of the ENE fault.

The rupture propagates bilaterally from the hypocenter with a slip rate not higher than 1 m/sec and is mainly confined to the shallow portion in the first 10 sec (Figure 12). Then it propagates to the deep portion in the northern part, while in the southern part, slip still occurs mainly in the shallow part, with a slip velocity of less than 1 m/sec. From 12 sec on, rupture propagates northward unilaterally. In the

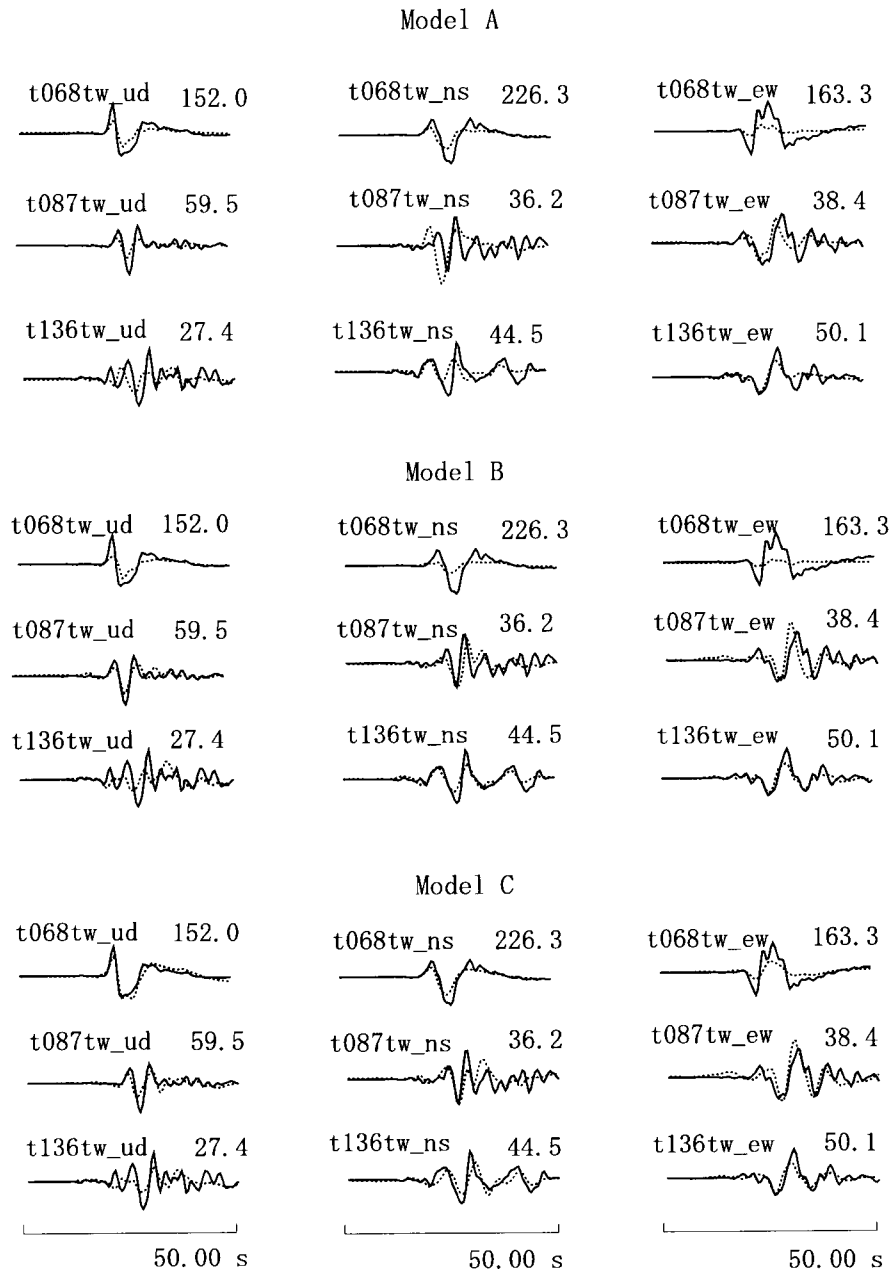


Figure 7. Comparison of synthetic (dotted line) and observation (solid line) waveform fittings for the three fault models.

north faulting area, the largest slip rate reaches 4.5 m/sec. Two separated asperities can be identified on the ENE fault. The deep one is an overlap of large slip observed across the +20 to +30 km area. The shallow one starts at 14 sec and lasts about 20 sec. The rupture propagates at an average velocity of 2.5 km/sec. Long rise time and large slip are two significant features of the mainshock (Fig. 10). A total moment of 2.7×10^{20} N m is released in about 40 sec. Summing up all focal mechanisms at each knot weighted by each seismic moment, we get the best double-couple solution, which has a nodal plane with strike of 16° , dip of 28° , and rake of 77° .

Discussion

We have obtained very large dislocations in the shallow faulting area by using a multifault model from the inversion of strong-motion waveform and the GPS data. Large ground motions, observed from both strong-motion data and GPS data in the northern part, are consistent with the large slip obtained in this study. Note that the largest slip occurs on the ENE fault, in the area where the highest concentrations of fatalities were reported. Our fitting result suggests the necessity of introducing the ENE fault; moreover, our result is consistent with the results of other research (Table 6).

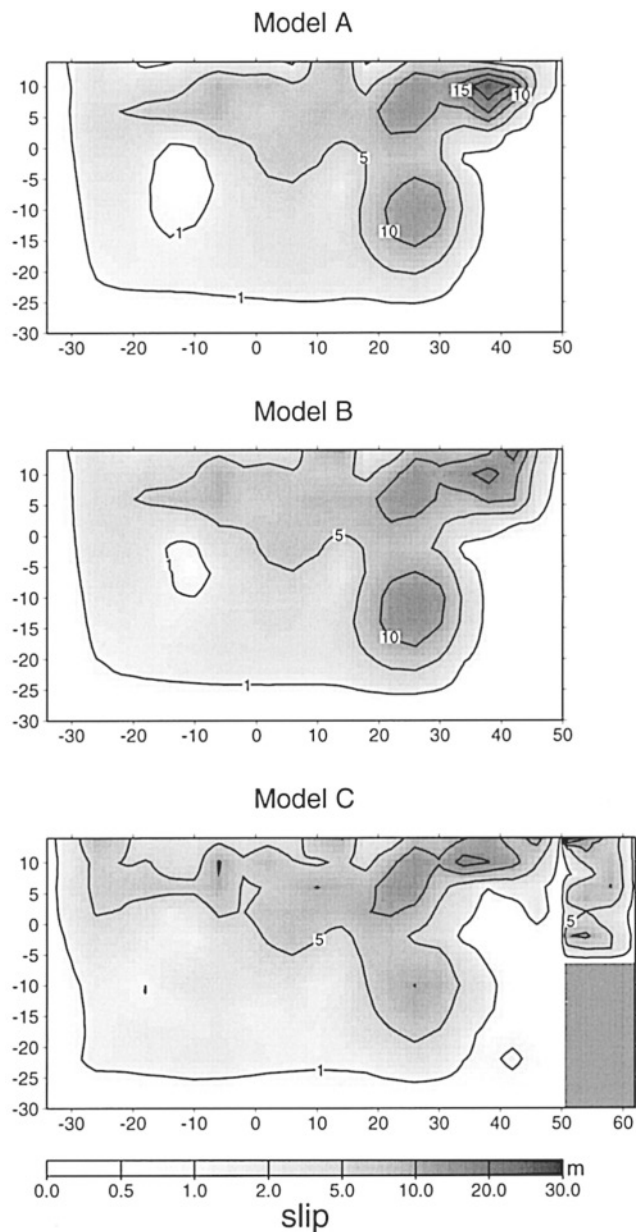


Figure 8. Comparison of slip distribution for the three fault models. The unit for the frame labels is km (the same in the following figure).

The Earthquake Research Institute (ERI), at the University of Tokyo, has deployed a temporary seismic network in central Taiwan since the beginning of October 1999. These temporary stations recorded a total of 740 earthquakes from 11 to 14 October, with magnitudes ranging from 0.7 to 4.8. Figure 13 shows the aftershock epicenter distribution (Dr. Shinichi Sakai, *et al.*, personal comm., 2000). Note that, except for some aftershocks located in the northern deep portion where large slip was obtained, there are no aftershocks in the area where large slip occurred, and aftershocks occurred mainly in marginal areas, as other studies have shown (e.g., Mendoza and Hartzell, 1988; Takeo, 1990). With a

close examination of a cross section map of the northern deep portion (Fig. 13), we can determine that aftershocks occurred under the assumed fault. We will continue this discussion after we analyze the relationship between the slip vectors and the ENE fault.

As we know, Taiwan lies on a collision boundary between the Eurasian plate and the Philippine Sea plate (Fig. 1). Mountain building in Taiwan is related to this collision. A wedge model (Suppe, 1981) approximates the mountain wedge as a thinly tapered wedge of Coulomb material at the failure threshold. But the wedge model does not account for deep orogenic processes identified recently by seismic tomography. More importantly, the wedge model lacks evidence supporting the subduction of the continental lithosphere under the Central Range, since no shallow events occurred in the Western Foothills before the Chi-Chi earthquake. Wu *et al.* (1997) proposed a lithospheric plate collision model to resolve the inconsistency. Lin and Roecker (1998) established an exhumation-collision model, which gives a possible mechanism for the lithospheric plate collision. However, there are still controversies about the physics of crustal exhumation. The Chi-Chi earthquake is a large shallow-thrust earthquake with large slip occurring mainly above 10 km, good evidence that the continental lithosphere is subducted under the Western Foothills. Therefore, the wedge model has no contradiction in the Western Foothills.

Both the wedge model and the lithosphere plate collision model predict a maximum compression stress normal to the Central Range in the mountain area. The strike direction of the Central Range hence reflects the direction of the regional compressive stress. North of latitude 24° N, the Central Range deflects to the east (Fig. 14, also noted by Wu [1978]). We believe this indicates the variation of regional tectonic stress in the mountain belt. The Longitudinal Valley, with a left-lateral movement (e.g., Allen, 1962), has been identified as a collision-transform boundary (e.g., Seno, 1977; Wu, 1978), which decouples the plate collision movement in the northwest direction into westward collision (mountain-building) and left-lateral movement along the valley area. The Longitudinal Valley terminates north of 24° N, suggesting a different collision pattern north of 24° N with the southern part. The GPS observations from 1990 to 1995 show that, although GPS velocity vectors of stations in southeast Taiwan trend in the direction of 306° to 322° with rates of 56–82 mm/yr. On the other hand, the deformation rates decay about 30 mm/yr discontinuously, and these directions turn westward at the western side of the Longitudinal Valley (Yu *et al.*, 1997). Deformation vectors in western Taiwan rotate northward gradually from south to north. Based on the results of Yu *et al.* (1997), it seems that the deformation vectors direct westward in the southern part, to NWW at 23.5° N, to NW at 24° N, and in a much more complex direction north to 24° N (Fig. 14). Unfortunately, there are too few stations in the northern part to determine the direction of the maximum principle stress. However, the Longitudinal Valley does not stretch further north than 24°

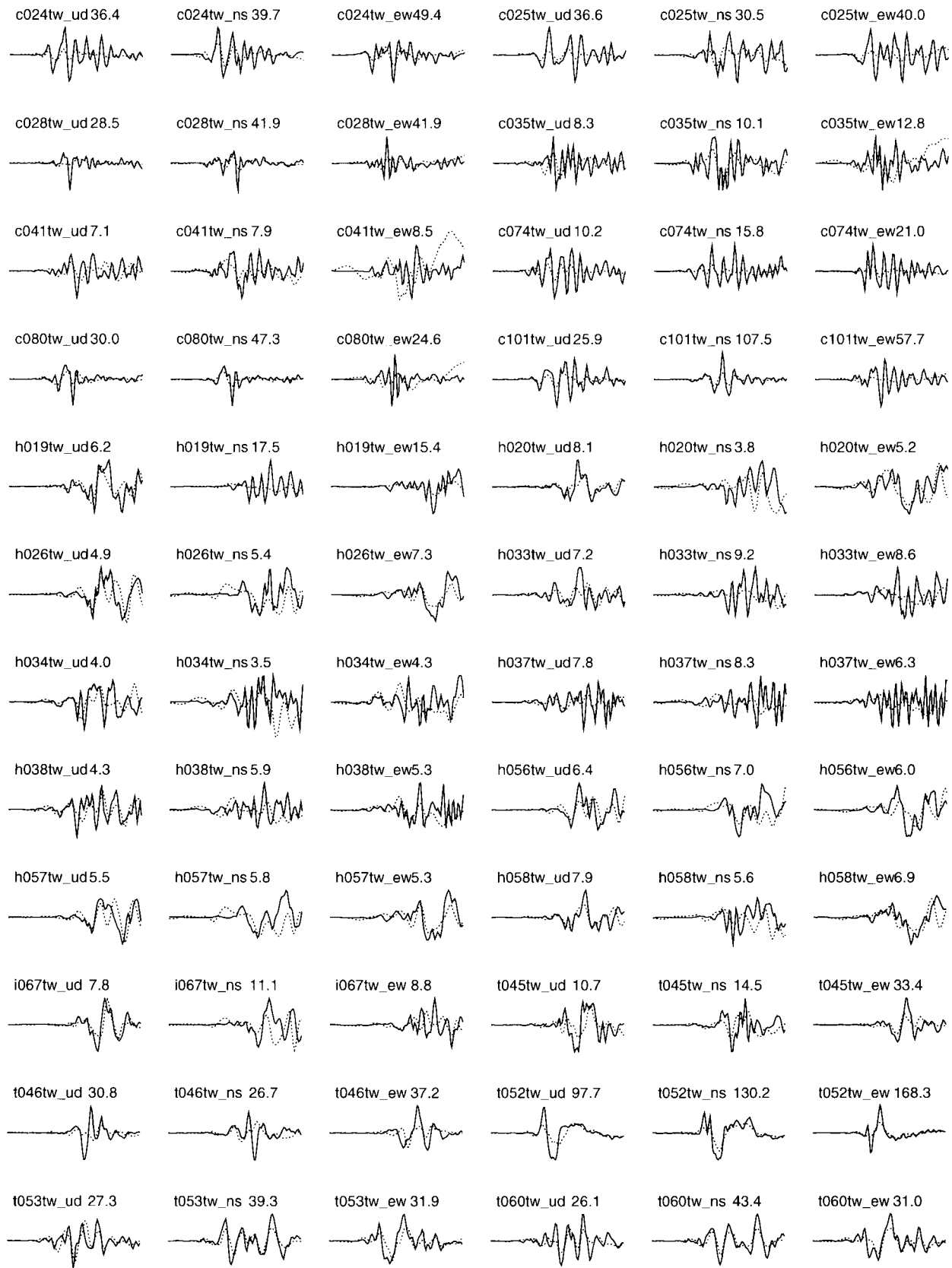


Figure 9. Synthetic (dotted line) and observed (solid line) waveform comparison for the final result. The maximum observed amplitudes are shown following the station codes. The unit is cm/sec.
(continued on following page)

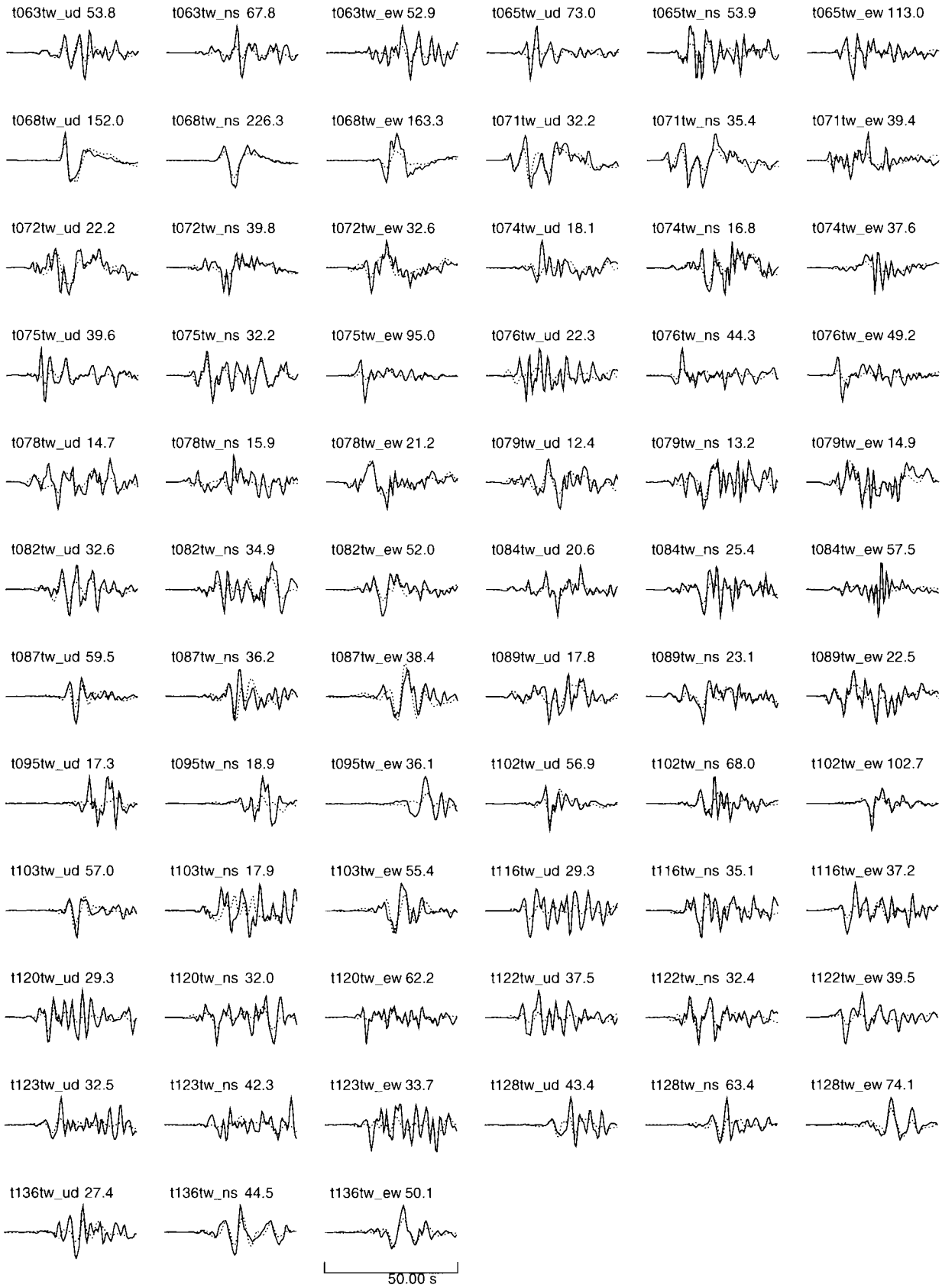


Figure 9. Continued.

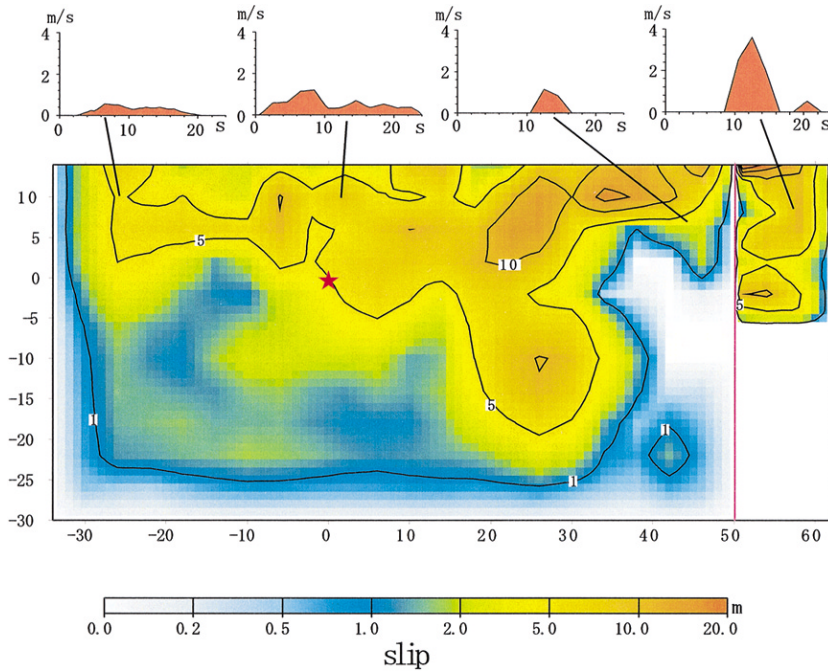


Figure 10. Slip distribution and slip rate graph of the final result. The red star means the hypocenter.

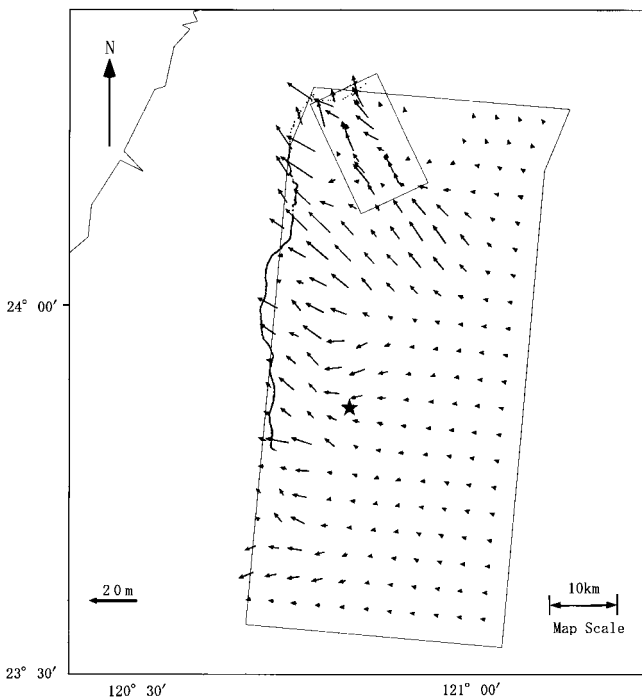


Figure 11. Slip vector map of the final result (symbols are the same as in Figure 6).

N. This indicates that the decoupling of the plate collision terminates in the northern side of the Longitudinal Valley. The slip vectors on the NNE fault and the ENE fault also indicate that the direction of the maximum principle stress turns from E–W to NW–SE. These results suggest a maximum principle stress approximately normal to the NNE strike

in the southern part but normal to the ENE strike direction in the most northern area.

We can further estimate the friction coefficient assuming a simple tectonic stress state. Our inversion result indicates that ruptures started at the hypocenter with mainly a dip-slip component. When the rupture propagates to the northern part, the faulting movement has a large strike-slip component due to changes in driving stresses. The thrusting faulting in the southern part suggests that in this area the minimum principle stress should be in a vertical direction. High pore pressure in this thin-skinned decollement structure (about 0.7 times hydrostatic) (Suppe, 1981) led to a small amount of effective stress in the vertical direction. According to the Coulomb-Mohr fracture criterion (Scholz, 1990), the dip angle can be related to the coefficient of internal friction (Fig. 15) as follows:

$$\delta = \frac{\pi}{4} - \frac{1}{2} \arctan \mu \quad (7)$$

With the dip angle $\delta = 30^\circ$ assumed for the NNE fault, from equation 7 we have the coefficient of internal friction $\mu = \tan 30^\circ = 0.57$ in the hypocenter area.

We attribute the slip rotations mainly to changes in regional tectonic stress. Assuming a maximum horizontal principle stress normal to the ENE strike in the north part instead of normal to the NNE strike, we can estimate the expected slip rotation angle on such a preexisting weak fault (i.e., the Chelungpu fault) as follows. Using the *P*-wave first motions and *SH/P* amplitude ratios, Rau *et al.* (1996) determined focal mechanisms of the small to moderate-size earthquakes occurring in western Taiwan and in the Central Range areas

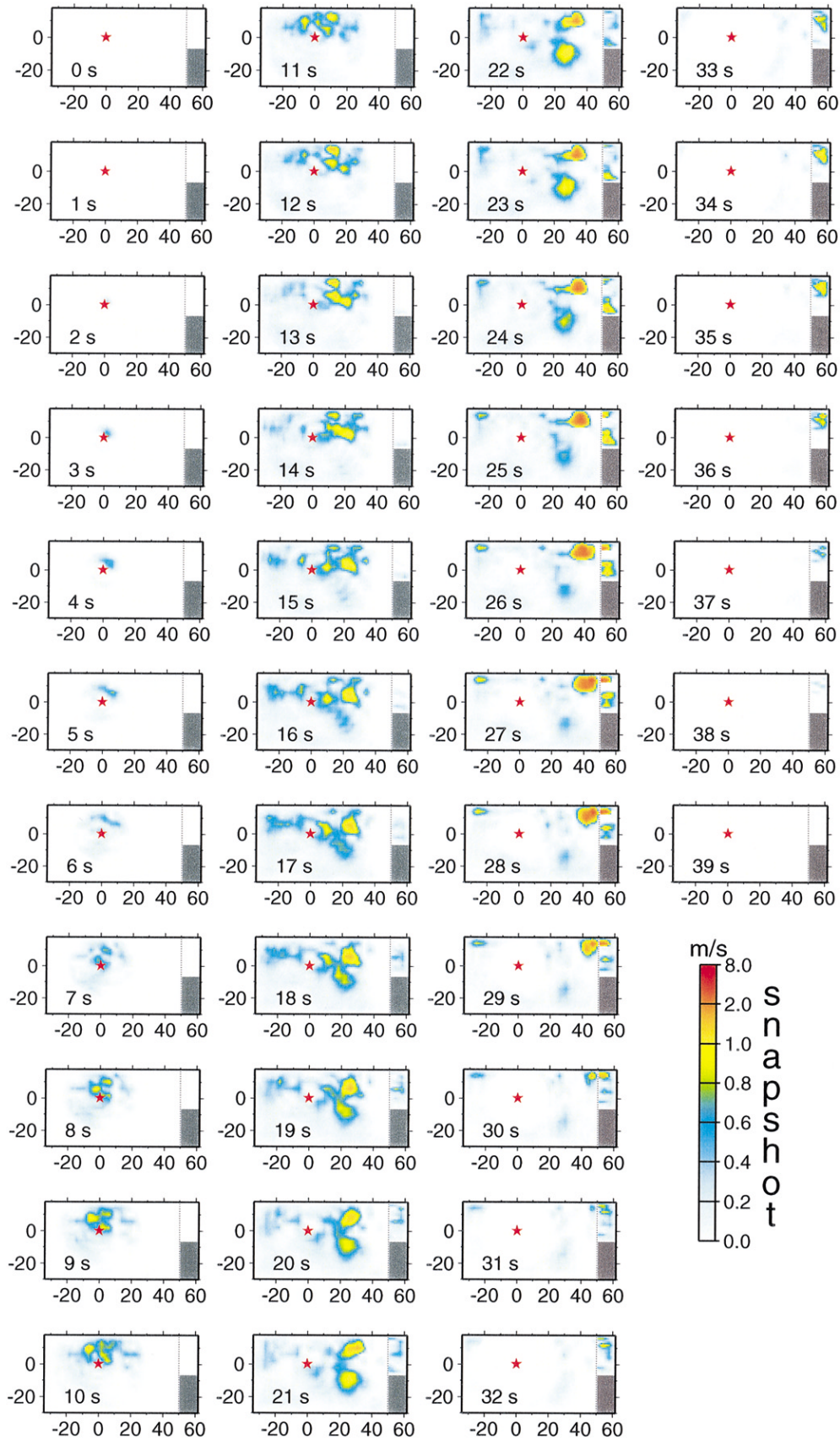


Figure 12. Snapshot (per second) of the source process.

Table 6
Double-Couple CMT Solutions of the Chi-Chi Earthquake

	Strike	Dip	Rake	Moment $\times 10^{20}$ N/m
USGS	357	29	67	2.4
ERI	44	39	114	2.5
HARVARD	26	27	82	4.1
This study	16	28	76	2.7

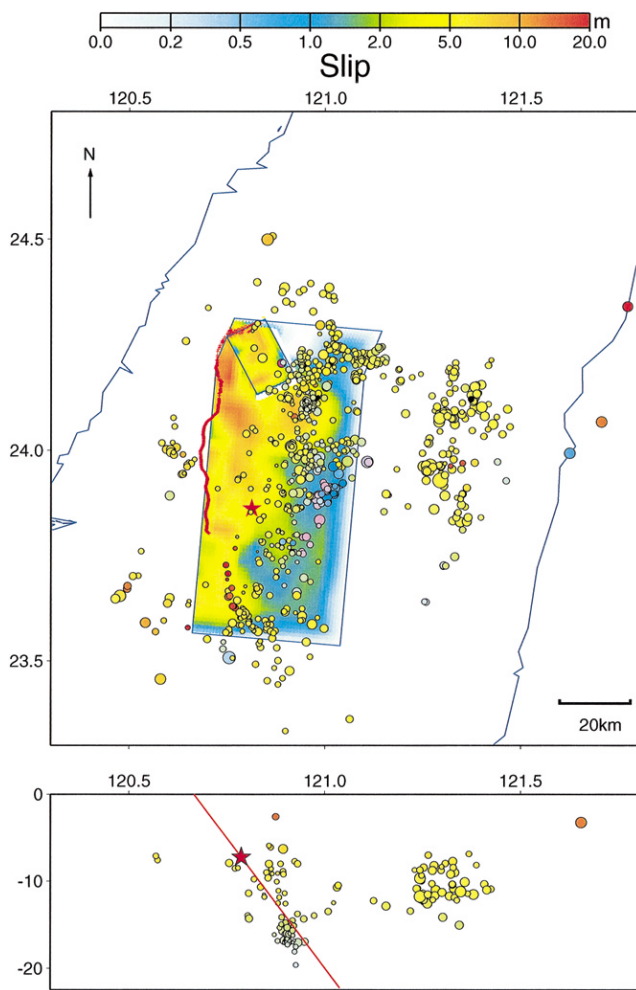


Figure 13. Slip distribution and aftershock (colored circle) distribution map. Colored circles correspond to different depths. The red asterisk indicates the epicenter of the Chi-Chi earthquake. The bold red line indicates the surface rupture trace. The lower box is the cross section along the southern fault edge (N85°W). For explicitness, only aftershocks located from 24° to 24.15° are shown in this figure, where we can clearly distinguish that aftershocks occurred under the assumed fault plane.

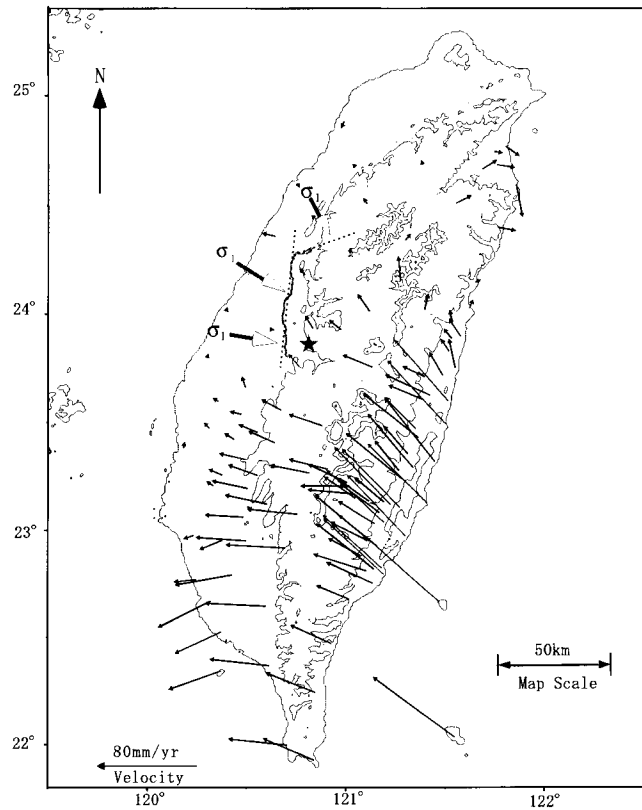


Figure 14. Variation of the maximum principle compression (σ_1 , in the horizontal direction) in the studied area and velocity field of GPS stations from 1990 to 1995 in Taiwan (after Yu *et al.*, 1997). Dotted lines indicate the NNE and the ENE faults respectively. The bold-dashed line shows the surface rupture trace. The epicenter of the mainshock is marked by a star.

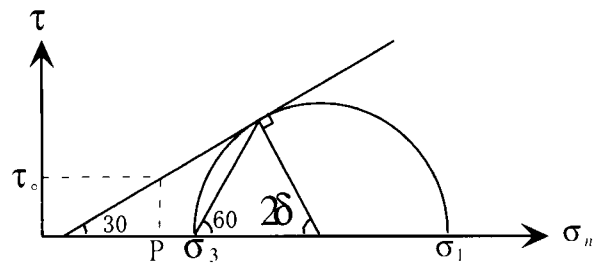


Figure 15. Illustration of the Coulomb-Mohr fracture criterion by a Mohr diagram. P, pore pressure, δ , dip angle of the fault plane; τ_0 , cohesion strength.

from 1991 to 1994. Their results show that the strike-slip and thrust faulting mechanisms are mixed in the background seismicity of western Taiwan. Therefore, we assume the principle stresses $\sigma_1 > \sigma_2 = \sigma_3 = \rho g z$ (σ_1 and σ_2 in the horizontal direction, σ_3 in the vertical direction), pore pressure $P = \lambda \sigma_3 = \lambda \rho g z$ ($\lambda = 0.7$), strike difference θ defined as the angle between the σ_2 direction and the fault strike, and dip angle δ , then net traction τ on this fault plane with a slip angle ϕ can be determined as follows:

$$\begin{aligned} \tau = & (\sigma_1 - \sigma_3) \cos \theta \sin \delta (\sin \theta \cos \phi \\ & + \cos \theta \cos \delta \sin \phi) - \mu [\sigma_1 \sin^2 \delta \cos^2 \theta \\ & + \sigma_3 (\sin^2 \delta \sin^2 \theta \\ & + \cos^2 \delta - \lambda)] \end{aligned} \quad (8)$$

The maximum traction on this NNE fault under such a stress state can be obtained when we let the derivative of traction (equation 8) with respect to ϕ equal zero, that is,

$$\tan \phi = \frac{\cos \theta \cos \delta}{\sin \theta}. \quad (9)$$

Since we assume σ_1 is normal to the N65°E strike in the northern part, for the N5°E fault $\theta = 60^\circ$, $\delta = 30^\circ$, and we have $\phi = 27^\circ$; if σ_1 is in the NW direction (N45°W, according to the GPS surveys by Yu [1997]), then $\theta = 40^\circ$, we have $\phi = 46^\circ$. The slip rake ranges around 40° in the northern part, indicating that the regional stresses in the northern part have a maximum principle stress in the direction of NW to NNW.

Let us continue discussing the effects of fault geometry. Consider the traction force on the NNE fault with a maximum principle stress in a NNW direction (N25°W), i.e., $\theta = 60^\circ$. According to (9), the rake angle with maximum traction is 27° . From equation 8, with $\mu = 0.57$ and $\lambda = 0.7$, we can estimate the maximum traction τ as

$$\tau = 0.20\sigma_1 - 0.35\sigma_3 \quad (10)$$

While traction on the ENE fault can be estimated using equation 8 ($\theta = 0^\circ$, $\delta = 25^\circ$ and $\lambda = 0.7$), as follows

$$\tau = 0.28\sigma_1 - 0.31\sigma_3 \quad (11)$$

Hence, traction on the NNE fault (equation 10) is less than 72% of that of the ENE fault (equation 11), given the maximum horizontal principle stress in the NNW direction. This suggests that the faulting of the NNE fault in the northern part is discouraged under such a stress state. Although large slip occurs in the northern part, rupture is inhibited from propagating northward due to the changes in tectonic stress. If there is a weakness fault striking in the ENE direction, a rupture on such a fault would be triggered. The observed ENE fault indicates the existence of a weak fault having an ENE strike. Rupture hence propagates in the ENE direction, and the largest slip occurs on the ENE fault.

Conclusions

The source process of the Chi-Chi earthquake has been determined by using a multifault model based on the inversion of strong-motion waveform data and GPS data. A total of 2.7×10^{20} N m were released in 40 sec, with an average rupture velocity of 2.5 km/sec during the mainshock. Aftershocks occurred mainly in areas where little or no slip oc-

curred. In most of the faulting area, the reverse component is dominant, especially in the southern area. However, slip vector rotation occurs in the northern part. The results show that large slip occurs mainly in the shallow section of the faulting area, while the rupture propagates to the deep northern part with strike-slip and dip-slip components, triggering faulting of the ENE fault. The largest slip (about 20 m) is obtained in the ENE fault, according to our inversion analysis. Long rise time and large slip are two significant features of the Chi-Chi earthquake.

We attribute the rotations of slip vectors in the northern part to changes in the complex tectonic stress shown by the GPS velocity field. The expected slip rotation under the complex tectonic stress is consistent with that obtained from our inversion analysis. Changes in regional tectonic stress discouraged northward propagation of ruptures. Therefore, in the north end, the rupture propagates to the ENE instead of northward.

Acknowledgments

We would like to express our gratitude to CWB for providing us with the strong-motion data.

References

- Akaike, H. (1980). Likelihood and the Bayes procedure, in *Bayesian Statistics*, J. M. Bernardo, M. H. DeGroot, D. V. Lindley, and A. F. M. Smith (Editors), University Press, Valencia, Spain, 143–166.
- Aki, K., and P. G. Richards (1980). *Quantitative Seismology: Theory and Methods*, W. H. Freeman, New York.
- Allen, C. R. (1962). Circum-Pacific faulting in the Philippines-Taiwan region, *J. Geophys. Res.* **67**, 4795–4812.
- Bonilla, M. G. (1999). A note on historic and Quaternary faults in western Taiwan, *U.S. Geol. Surv. Open-File Rept.* 99-447.
- Bouchon, M. (1981). A simple method to calculate Green's functions for elastic layered media, *Bull. Seism. Soc. Am.* **71**, 959–971.
- Central Geological Survey (1999). Report of geological survey on the Chi-Chi earthquake, Table 5-1, <http://www.moeacgs.gov.tw/CGSWeb/Result/Fault/921/921a/S-17.htm> Yoshioka (last accessed 23 July 2001).
- Chen, Y. L. (1995). Three-dimensional velocity structure and kinetic analysis in Taiwan area, *Master D. Thesis*, National Central University, Taipei, Taiwan.
- Chiu, H. C. (1997). Stable baseline correction of digital strong-motion data, *Bull. Seism. Soc. Am.* **87**, 932–944.
- Chung, J., and Y. Yeh (1997). Shallow crustal structure from short-period Rayleigh-wave dispersion data in Southwestern Taiwan, *Bull. Seism. Soc. Am.* **87**, 370–382.
- Hartzell, S., and T. H. Heaton (1983). Inversion of strong ground motion and teleseismic waveform data for the fault rupture history of the 1979 Imperial Valley, California, earthquake, *Bull. Seism. Soc. Am.* **73**, 1553–1583.
- Hartzell, S., and T. H. Heaton (1986). Rupture history of the 1984 Morgan Hill, California, earthquake from the inversion of strong motion records, *Bull. Seism. Soc. Am.* **76**, 649–674.
- Hartzell, S., P. Liu, and C. Mendoza (1996). The 1994 Northridge, California, earthquake: inversion of rupture velocity, risetime, and high-frequency radiation, *J. Geophys. Res.* **101**, 20,091–20,108.
- Ide, S., and M. Takeo (1997). Determination of constitutive relations of fault slip based on seismic wave analysis, *J. Geophys. Res.* **102**, 27,379–27,391.

- Ide, S., M. Takeo, and Y. Yoshida (1996). Source process of the 1995 Kobe earthquake: determination of Temporal slip distribution by Bayesian modeling, *Bull. Seism. Soc. Am.* **86**, 547–566.
- Iwan, W. D., M. A. Moser, and C. Y. Peng (1985). Some observations on strong-motion earthquake measurement using a digital accelerograph, *Bull. Seism. Soc. Am.* **75**, 1225–1246.
- Kao, H., and R. J. Rau (1999). Detailed structures of the subducted Philippine Sea plate beneath northeast Taiwan: a new type of double seismic zone, *J. Geophys. Res.* **104**, 1015–1033.
- Kennet, L. N., and N. J. Kerry (1979). Seismic waves in a stratified half space, *Geophys. J. R. Astr. Soc.* **57**, 557–583.
- Lin, C. H., and S. W. Roecker (1998). Active crustal subduction and exhumation in Taiwan, in *When Continents Collide: Geodynamics and Geochemistry of Ultrahigh-Pressure Rocks*, B.R. Hacker and J. G. Liou (Editors), Kluwer Academic Publishers, The Netherlands, 1–25.
- Liu, K. S., T. C. Shin and Y. B. Tsai (1999). A free-field strong motion network in Taiwan: TSMIP, *TAO* **10**, 377–396.
- Ma, K. F., C. T. Lee, and Y. B. Tsai (1999). The Chi-Chi, Taiwan earthquake: large surface displacements on an inland thrust fault, *EOS Trans. Am. Geophys. Union* **80**, 605.
- Mendoza, C., and S. H. Hartzell (1988). Aftershock patterns and mainshock faulting, *Bull. Seism. Soc. Am.* **78**, 1438–1449.
- Okada, Y. (1992) Internal deformation due to shear and tensile faults in a half-space, *Bull. Seism. Soc. Am.* **82**, 1018–1040.
- Rau, R. J., F. T. Wu, and T. C. Shin (1996). Regional network focal mechanism determination using 3D velocity model and SH/P amplitude ratio, *Bull. Seism. Soc. Am.* **86**, 1270–1283.
- Scholz, C. H. (1990). *The Mechanics of Earthquakes and Faulting*, Cambridge University Press, New York.
- Seno, T. (1977). The instantaneous rotation vector of the Philippine Sea plate relative to the Eurasian plate, *Tectonophysics* **42**, 209–226.
- Seno, T. (1993). A model for the motion of the Philippine Sea plate consistent with Nuvel-1 and geological data, *J. Geophys. Res.* **98**, 17,941–17,948.
- Shin, T. C., K. W. Kuo, W. H. K. Lee, T. L. Teng, and Y. B. Tsai (2000). A preliminary report on the 1999 Chi-Chi (Taiwan) earthquake, *Seism. Res. Lett.* **71**, 23–29.
- Suppe, J. (1981). Mechanics of mountain building and metamorphism in Taiwan, *Memo. Geol. Soc. China* **4**, 67–89.
- Takeo, M. (1985). Near-field synthetic seismograms taking into account the effect of anelasticity, *Meteorol. Geophys.* **36**, 245–257.
- Takeo, M. (1987). An inversion method to analyze the rupture processes of earthquakes using near-field seismograms, *Bull. Seism. Soc. Am.* **77**, 490–513.
- Takeo, M. (1990). Fault heterogeneity of inland earthquakes in Japan, *Bull. ERI. Univ. of Tokyo* **65**, 541–569.
- Takeo, M. (1992). The rupture process of the 1989 Offshore Ito earthquakes preceding a submarine volcanic eruption, *J. Geophys. Res.* **97**, 6613–6627.
- Tsai, Y. B. (1986). Seismotectonics of Taiwan, *Tectonophysics* **125**, 17–37.
- Wu, F. T. (1978). Recent tectonics of Taiwan, *J. Phys. Earth* **26**, 265–299.
- Wu, F. T., R. J. Rau, and D. Salzberg (1997). Taiwan orogeny: thin-skinned or lithospheric collision? *Tectonophysics* **274**, 191–220.
- Yoshida, S. (1992). Waveform inversion for rupture process using a non-flat seafloor model: application to 1986 Andean of Islands and 1985 Chile earthquakes, *Tectonophysics* **211**, 45–59.
- Yu, S. H., H. Y. Chen, and L. C. Kuo (1997). Velocity field of GPS stations in the Taiwan area, *Tectonophysics* **274**, 41–59.
- Yu, S. B., L. C. Kuo, R. S. Punongbayan, and E. G. Ramos (1999). GPS observation of crustal deformation in the Taiwan-Luzon region, *Geophys. Res. Lett.* **26**, 923–926.

Earthquake Research Institute
University of Tokyo
1-1-1 Yayoi, Bunkyo, Tokyo, 113 Japan
wuchang@eri.u-tokyo.ac.jp
takeo@eri.u-tokyo.ac.jp
ide@eri.u-tokyo.ac.jp

Manuscript received 31 July 2000.